

UDC: 62-523.2, 621.865.8, 007.52

## Design, modeling, and control of a variable stiffness joint based on a torsional magnetic spring

I. V. Shardyko<sup>a</sup>, V. M. Kopylov, K. A. Volnyakov

RTC,  
21 Tikhoretsky prospect, Saint Petersburg, 194064, Russia

E-mail: <sup>a</sup> i.shardyko@rtc.ru

*Received 27.01.2023, after completion – 27.04.2023.  
Accepted for publication 21.06.2023.*

Industrial robots have made it possible for robotics to become a worldwide discipline both in economy and in science. However, their capabilities are limited, especially regarding contact tasks where it is required to regulate or at least limit contact forces. At one point, it was noticed that elasticity in the joint transmission, which was treated as a drawback previously, is actually helpful in this regard. This observation led to the introduction of elastic joint robots that are well-suited to contact tasks and cooperative behavior in particular, so they become more and more widespread nowadays. Many researchers try to implement such devices not with trivial series elastic actuators (SEA) but with more sophisticated variable stiffness actuators (VSA) that can regulate their own mechanical stiffness. All elastic actuators demonstrate shock robustness and safe interaction with external objects to some extent, but when stiffness may be varied, it provides additional benefits, e. g., in terms of energy efficiency and task adaptability. Here, we present a novel variable stiffness actuator with a magnetic coupler as an elastic element. Magnetic transmission is contactless and thus advantageous in terms of robustness to misalignment. In addition, the friction model of the transmission becomes less complex. It also has milder stiffness characteristic than typical mechanical nonlinear springs, moreover, the stiffness curve has a maximum after which it descends. Therefore, when this maximum torque is achieved, the coupler slips, and a new pair of poles defines the equilibrium position. As a result, the risk of damage is smaller for this design solution. The design of the joint is thoroughly described, along with its mathematical model. Finally, the control system is also proposed, and simulation tests confirm the design ideas.

**Keywords:** robotics, design, control system, series elastic actuators, variable stiffness actuators, magnetic spring, elastic structure preserving control

Citation: *Computer Research and Modeling*, 2023, vol. 15, no. 5, pp. 1323–1347.

This work was supported by the Ministry of Science and Higher Education of the Russian Federation. State assignment No. 075-01595-23-00 (FNRG-2022-0009, ID 1021060307688-8-2.2.2).

УДК: 62-523.2, 621.865.8, 007.52

## Разработка конструкции, моделирование и управление шарниром с переменной упругостью на основе магнитной пружины кручения

И. В. Шардыко<sup>а</sup>, В. М. Копылов, К. А. Волняков

ЦНИИ РТК,

Россия, 194064, г. Санкт-Петербург, Тихорецкий проспект, д. 21

E-mail: <sup>а</sup> i.shardyko@rtc.ru

*Получено 27.01.2023, после доработки — 27.04.2023.*

*Принято к публикации 21.06.2023.*

С появлением промышленных роботов робототехника приобретает значение во всемирном масштабе как в экономике, так и в науке. Однако, их возможности сильно ограничены, особенно в части выполнения контактных задач, в которых есть необходимость регулирования или по крайней мере ограничения усилия в контакте. В определенный момент было замечено, что упругость в механической цепи шарнира, считавшаяся ранее негативным фактором, в этом отношении напротив является полезной. Данное наблюдение привело к появлению роботов с упругими шарнирами, пригодных к выполнению контактных задач и кооперативной деятельности в частности, в результате чего их распространение сегодня становится всё шире. Многие исследователи стремились реализовать подобные устройства не только в виде простейших последовательных упругих приводов, но и посредством более сложных шарниров с переменной упругостью (ШПУ), способных изменять собственную механическую жесткость. Все упругие шарниры обеспечивают в определенной мере устойчивость к ударным нагрузкам и безопасность взаимодействия с объектами внешней среды, однако изменение жесткости позволяет получить дополнительные преимущества, такие как энергоэффективность и адаптируемость к задачам.

В настоящей статье представлена новая реализация ШПУ, с магнитной муфтой в качестве упругого элемента. Магнитная передача является бесконтактной, и потому обладает преимуществом с точки зрения снижения чувствительности к смещению и рассогласованию осей. Описание модели трения также упрощается. Кроме того, данная муфта обладает характеристикой жесткости, которая не только не возрастает резко с повышением нагрузки, но становится более плавной, и даже снижается после точки максимума. Вследствие этого, при достижении максимального момента, муфта проскальзывает, после чего положение равновесия уже определяется новой парой полюсов. В итоге данное решение снижает риск механического повреждения. В статье подробно рассмотрен процесс разработки шарнира, представлена его математическая модель. Также предложена реализация системы управления шарниром и проведено компьютерное моделирование, подтверждающее принятые в разработке решения.

**Ключевые слова:** робототехника, разработка конструкции, система управления, приводы с последовательной упругостью, приводы с переменной упругостью, магнитные пружины, управление с сохранением упругой структуры

Работа выполнена в рамках выполнения государственного задания Минобрнауки России на 2023 год № 075-01595-23-00 «Исследования конструкций и разработка методов управления мехатронными узлами с переменной жесткостью» (FNRG-2022-0009, регистрационный номер 1021060307688-8-2.2.2).

## Introduction

In the last decades there has been a transition in the application of robots in industry and other areas, i. e., besides simple position tasks that can be precomputed, robots now execute more and more contact tasks. These tasks may turn out to have been planned beforehand with specified contact forces or be unforeseen but still the robot should be safe towards the environment and itself and also show some specified behavior during the contact. From the point of design this transition is expressed by introducing elasticity into robotic joints, which simplifies the torque measurement and force-torque control [Pratt, Williamson, 1995]. Yet, mere constant springs limit the performance of the robots, because some part of stiffness should be implemented virtually by the controller in order to vary the effective stiffness in contact. In response to this, variable stiffness actuators, or VSAs, were introduced [Migliore, Brown, DeWeerth, 2005; Tonietti, Schiavi, Bicchi, 2005], capable of varying stiffness mechanically over a relatively wide range. In addition, the variability of the stiffness characteristics allows one to adapt the system to tasks of a mechanical level. For this so-called task embodiment, the joint stiffness is tuned such that minimal active control influence is necessary to achieve a task [Petit, 2014]. However, to control simultaneously position (or torque) and stiffness, such a device should comprise at least two drives, consequently, the joints grow in mass, size and cost to provide the same power. This compromise still hinders strongly the propagation of VSAs in commercial robotics.

Plenty of actuators have been proposed in the last two decades and much more are still proposed every year [Wang et al., 2016; Liu et al., 2021]. A number of attempts have been made to classify them systematically [Vanderborgh et al., 2013], but the most noteworthy feature is the layout of the motors, which also defines their function. Thus, there are two types of actuators: uniform, or agonistic-antagonistic (VSA<sub>aa</sub>), and hybrid, or independent (VSA<sub>in</sub>). The structural schemes of both types are shown in Fig. 1, *a* and 1, *b* respectively. Uniform layout assumes that the joint contains two drives that operate in the same way, so that their co-motion changes the equilibrium position of the joint output, and the counter-motion changes stiffness, while the equilibrium position remains the same. In contrast, in independent joints one drive is responsible for the output motion while the other, for the stiffness variation.

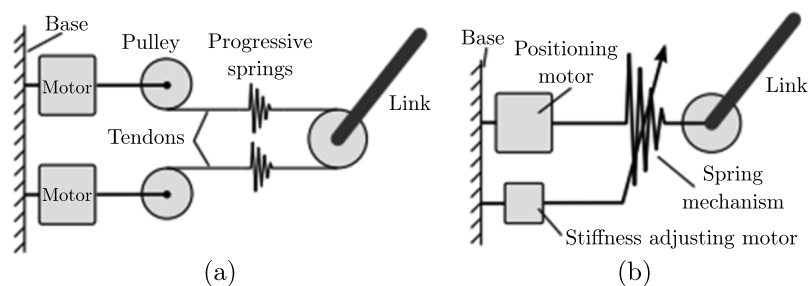


Figure 1. Two types of VSA joint structure: a) uniform design, b) independent design

The key part of the VSA is its stiffness regulation mechanism that can be based on different physical principles. There are tendon-based mechanisms [Migliore, Brown, DeWeerth, 2005], pneumatic mechanisms [Sun et al., 2021], purely mechanical geared mechanisms and also magnetic ones. A great number of prototypes use pure mechanics in different ways, many of which are referenced in reviews [Ham et al., 2009; Wolf et al., 2015]. Magnetic and electromagnetic mechanisms are rare to be found even if we take into account those that are combined with some mechanical transmission. Still, a brief review is required to encompass the main development trends.

Many authors present magnetic springs as variable stiffness mechanism, such as [Hyun et al., 2007]. The magnet has the ring structure as shown in Fig. 2. At first, only two rings were used, the

inner for rotor and the outer for stator. But later the authors modified the spring into a three-ring structure with a rotor magnet between the two stator ones. The variation of the overlap area leads to stiffness variation. A robotic joint has been designed based on this variable stiffness unit (VSU) [Choi et al., 2008], its structure and photo are shown in Fig. 3. The technical data for this joint are limited, only its limit torque and mass are known, which are  $10 \text{ N} \cdot \text{m}$  and  $0.538 \text{ kg}$ , respectively.

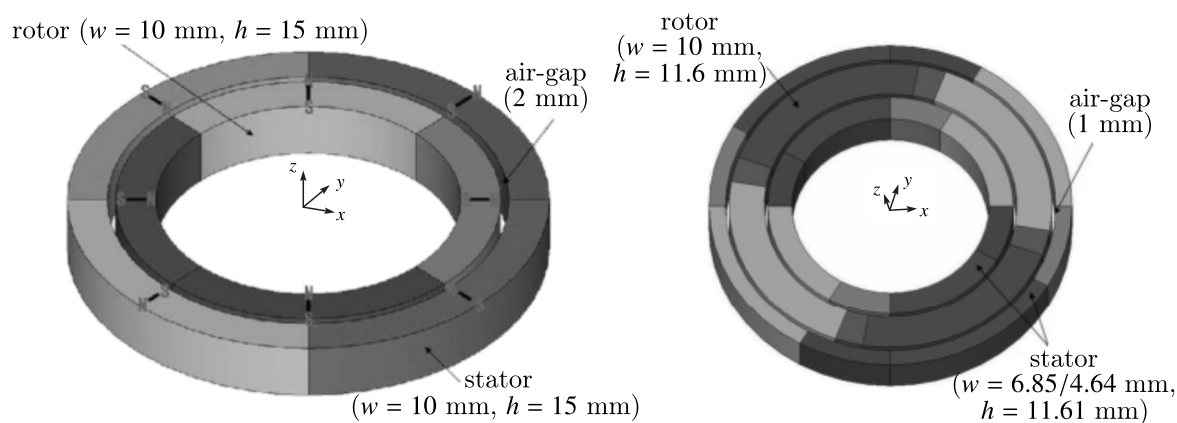


Figure 2. Spring layouts of the VSU joint: initial PM-type and optimal design shape of 3-rings PM-type.  $w$  is width,  $h$  is height

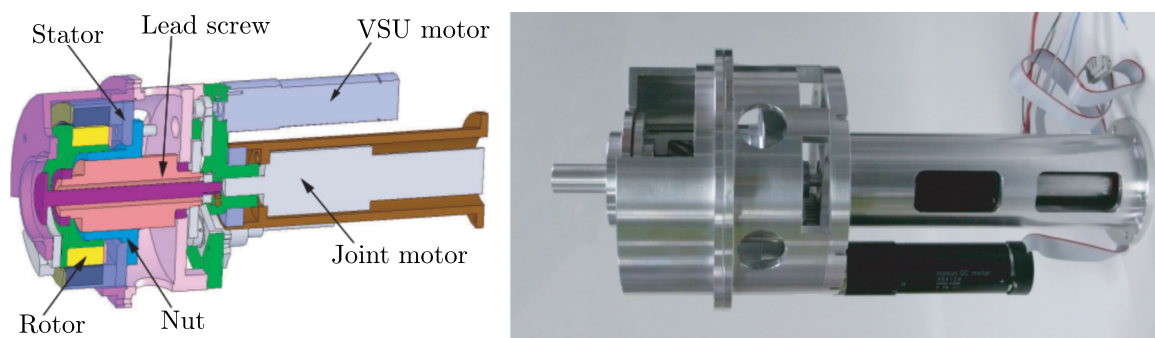


Figure 3. Design structure and the prototype of the variable stiffness joint [Choi et al., 2008]

A similar magnetic spring was presented in [Hossain et al., 2021]. It also has the three-ring structure, as shown in Fig. 4 (left), however, the stator is now between the two rotor layers. Another interesting feature is that the rotor is magnetized radially, while the stator is magnetized axially, as shown in Fig. 4 (right). The spring is not designed for application in robotics, but since it is analogous to the previous spring, it can be implemented if needed.

In contrast to the above-mentioned permanent magnet springs, in the joint named VSA-EM [Yang, Jang, Van Der Kooij, 2019] the spring is a coupler of electromagnetic nature that consists of a magnetic rotor and a stator combining a permanent magnet with electromagnetic winding. The working principle and the joint structure are shown in Fig. 5. The authors consider different ratios of magnetic and electromagnetic poles. Permanent magnets provide higher torque, no-current load bearing and higher stiffness, but also higher cost. The coupler itself is a stiffness variation actuator as the stiffness is controlled by current. Unfortunately, no technical data are provided.

Other prototypes comprise both magnetic and mechanical elastic elements. In [Pirooz et al., 2014] the proposed  $M^2$ -VSA has three elastic stages, and the magnetic spring is located between mechanical ones. The photos of the stages and the whole joint are presented in Fig. 6. A robotic arm

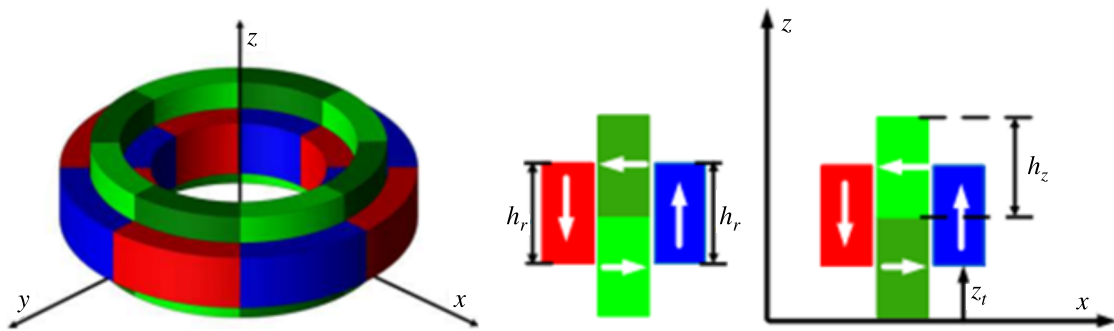


Figure 4. Perspective view and cut-through view of the 4-pole-pair dual-airgap coaxial spring VSMS.  $h_r$  – rotor height,  $h_z$  – stator half-height,  $z_r$  – rotor axial coordinate

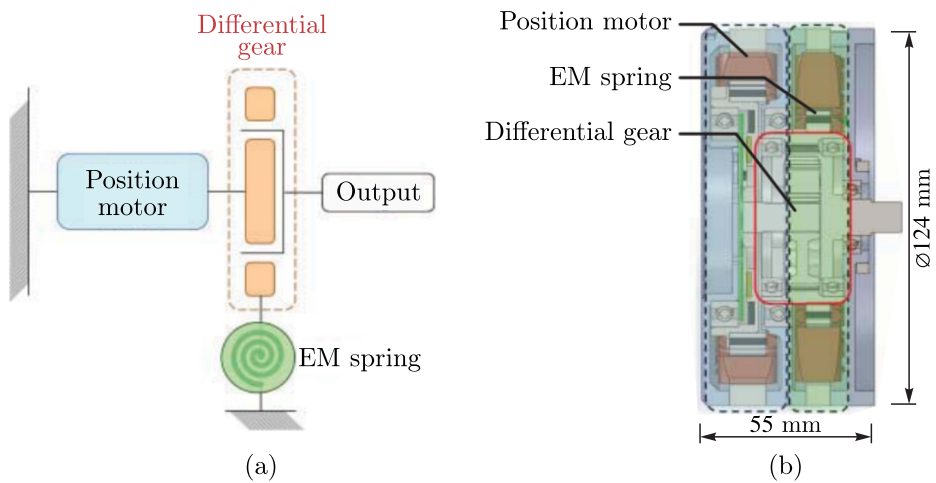


Figure 5. EM spring VSA design. (a) Connection between components. (b) Component arrangement and structure design

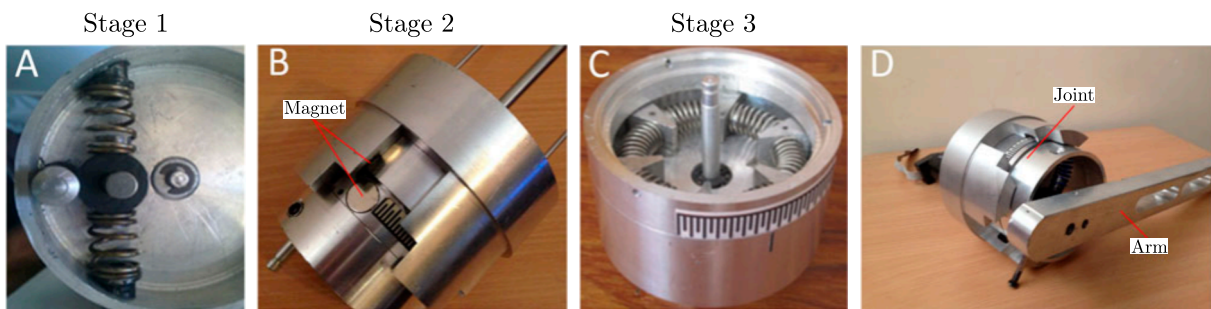


Figure 6. Design of  $M^2$ -VSA Joint. Spring set for stage 1 (A), magnets for stage 2 (B), spring set for stage 3 (C), and joint and attached arm (D)

with  $M^2$ -VSA joint would be able to safely interact with human operators and work under hazardous conditions thanks to the adjustment of the joints' stiffness and mitigation of the effect of impact. The motivation of the proposed design is to use mechanical and magnetic components to increase the load capacity and enhance the sensitivity and fast response.

Another joint named VSJPMM was presented in [Zhang et al., 2018]. The joint follows the agonistic-antagonistic paradigm, where both motion channels contain permanent magnet sliding springs. Figure 7 shows the photos of one spring and the joint. The magnetic springs have constant

stiffness, but the stiffness of the whole structure can be changed through the triangle tendon-pulley mechanism. The choice of the magnetic spring is justified by the wider variable-stiffness range, however, the comparison is made with some specific mechanical spring. Further articles developed the topic of this one, but they revealed the issues of control system mostly, while no technical data were given yet about the joint [Zhang et al., 2021]. A similar concept is implemented in CSMS [Olaru, Petrescu, Arcire, 2021], which is another translational spring, but partly electromagnetic. It is supposed that this spring is part of some bigger mechanism, which can be either uniform or independent. A scheme of the spring is depicted in Fig. 8. No data are provided either.

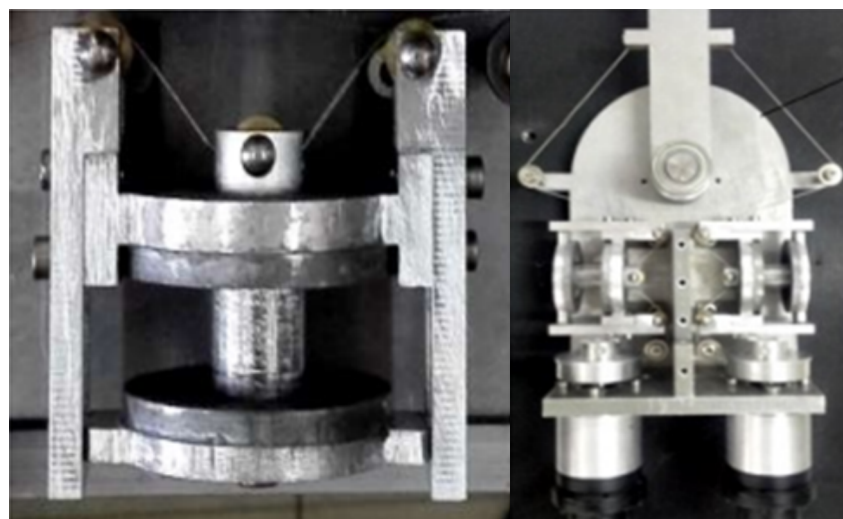


Figure 7. VSJPM joint: variable stiffness mechanism structure and joint prototype

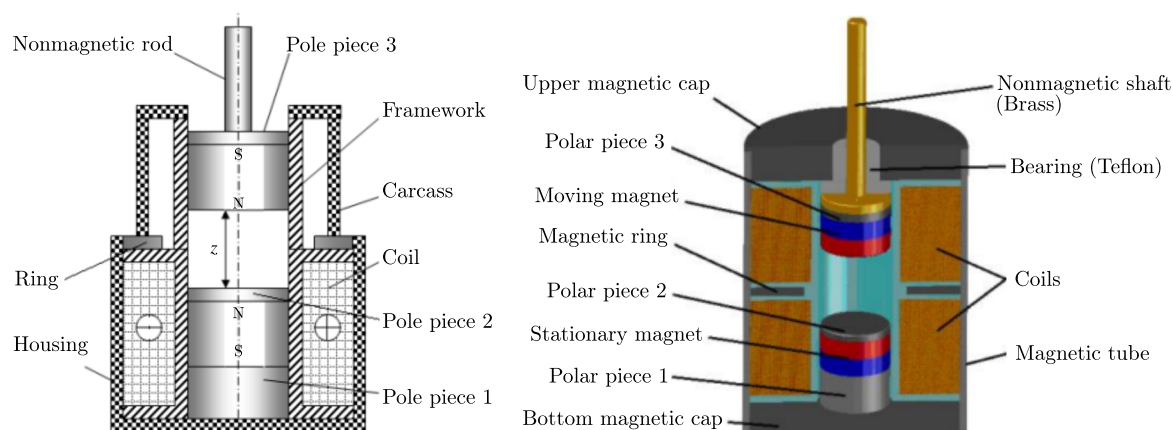


Figure 8. CSMS mechanism: conceptual model of CSMS and design of CSMS prototype using a single coil

This brief review shows that magnetic springs are readily implemented in both joint types, VSAAa and VSAin. The advantages of magnets include not only the lack of friction, but also the reduction of wobbling and loads due to misalignment. It is also important that the stiffness curve is almost linear in some part of the deflection range, which is usually about 50%. Hence, the control system design simplifies substantially. Moreover, when the load torque exceeds the limit, the magnet switches its poles (slips), which is undesirable because the static equilibrium position changes, but still it is better than the breakage of the gear or other transmission parts.

Magnetic contactless couplers have been known for quite a long time and there are two types of them: radial (see, e. g., Figs. 2, 4) or with end clearance. The air gap is a thin tube between the rotor and the stator in the former case, and a thin disc in the latter case. The volume that they require and their masses are approximately the same but the radial ones have a smaller diameter, while those with end clearance have a smaller length. The stiffness variation principle is different as well, which is the overlap area or air gap thickness, respectively. The change in stiffness due to air gap thickness is much more sensible when the gap is small, but to achieve this, required extremely fine motions of the rotor are required because the magnetic forces are inversely proportional to the cube of the distance between the centers of the magnets. In order to make the adjustment process smoother, we suggest using a magnetic coupler of the conical air gap, which is a kind of a hybrid solution, so the slope of the magnets to the axis is nonzero. The article is organized as follows. The design of the magnetic spring and its mathematical model are presented in Section II. Then, the overall joint design is given in Section III. Section IV shows the main steps of the controller development which is tested in simulation in Section V. Section VI concludes the article and outlines the future work.

## The design of the magnetic spring

The proposed magnetic coupler consists basically of two rings (may be considered as the rotor and the stator) with a number of permanent magnets placed on them. The analytical design of the magnets is performed on the basis of the equivalent solenoid method [Pyatin, 1980]. This method is workable only for magnetically hard materials such as ferrites and rare earth alloys, but it is exactly these materials that are used to manufacture strong permanent magnets. The condition of equivalency for a solenoid and a magnet is the equality of their magnetic torques, which leads to the magnetization equality provided that the distance between the magnet poles is equal to the length  $l$  of the equivalent solenoid and the pole area is equal to the area  $S$  of the equivalent solenoid coil. Then the equivalent current in a single-coiled solenoid is

$$i = Ml, \quad (1)$$

where  $M$  is material magnetization.

Usually the magnetic field at the center of the magnet end is specified for magnets in datasheets. For planar magnets the magnetic field at the center of the magnet end is roughly equal to the magnetic field at the magnet center and can be found as

$$B_0 = \frac{\mu_0 i}{d}, \quad (2)$$

where  $\mu_0$  is the magnetic constant and  $d$  is the magnet diameter.

This expression may be used to find the magnetization for a planar magnet, however, it is more convenient to use the equivalent current value which is justified for the case when  $l < d$ . The analysis of the magnet of a particular form is performed under the assumption that the magnet is replaced by a solenoid with the current flowing at its perimeter. It is important that the solenoid is placed at the center of the magnet thickness, i. e., between the poles.

The analysis involves two steps. The first step is to calculate the magnetic field that is induced by the currents of all the equivalent solenoids that are the part of the magnetic coupler on the elements of the current circuit of the chosen solenoid. The second step is calculate Ampere's force by which the magnetic field affects the element of the current circuit followed by integration of this force around the circuit. As a result, the force is found by which the field affects any single magnet of the coupler. The analysis is repeated for each magnet of both the rotor and the stator. The torque caused by magnetic forces is in fact the torque transmitted by the coupler.

The solenoid circuit is broken down into elementary segments for the analysis with corresponding currents  $i$ . The magnetic field for such a circuit can be found based on the Biot–Savart law:

$$d\mathbf{B} = B_0 \frac{d \, dl \times (r_0 - r)}{|r_0 - r|^3}, \quad (3)$$

where  $B_0$  is the field magnitude at the center of the magnet pole (certified, 1...1.3 Tl for most available magnets),  $d$  is the equivalent magnet diameter,  $dl$  is the circuit segment,  $r_0$  is the radius vector from the field source, and  $r$  is the radius vector of the circuit segment.

The equivalent diameter for a magnet of rectangular shape can be found as

$$d = \frac{ab}{\sqrt{a^2 + b^2}}, \quad (4)$$

where  $a$  and  $b$  are the rectangular sides.

The force acting on the current circuit can be found as

$$\mathbf{F} = \frac{B_0 d}{\mu_0} \oint dl \times \sum d\mathbf{B}, \quad (5)$$

where addition is performed for the chosen circuit segment  $dl$  from all the field sources that the analysis takes into account, including the element  $dl$  itself for which  $d\mathbf{B}$  is zero.

Large values of  $B_0$  that are typical for rare-earth metal permanent magnets provide large magnetic force  $F$ , and due to this fact the average air gap radius required for the joint torque transmission is comparable with the flexible spline radius of the harmonic gear.

As the magnet shape can be described by a set of line segments, all the integral expressions in the analysis above can be calculated explicitly. However, the expressions would be bulky for implementation. For this purpose, the torque-angle relationship has been determined and then approximated by the cubic polynomial with the coefficient of determination  $R^2 = 0.9951$  (see Fig. 9).

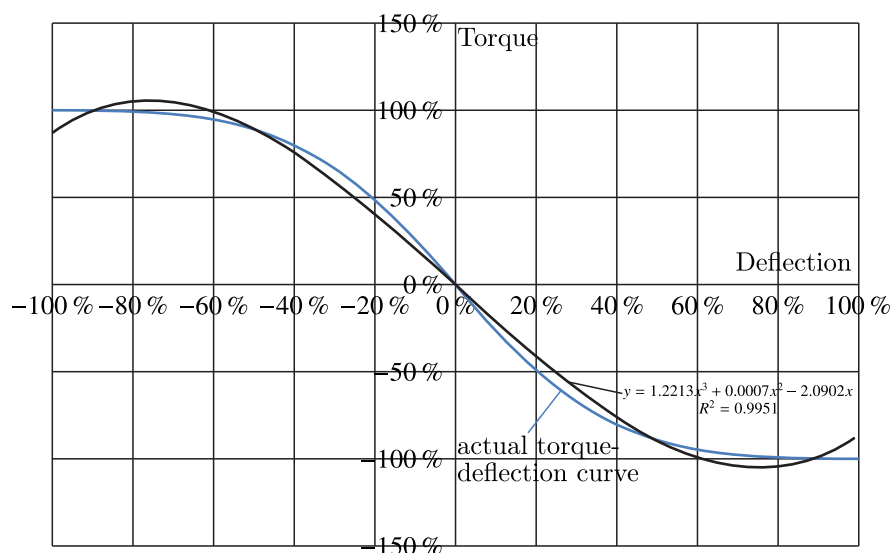


Figure 9. Torque – deflection curve of the magnetic coupler

The coordinates in Fig. 9 are relative. Deflection of 100% means that the center of the rotor magnet pole is located exactly between the stator magnets. Further rotor motion would cause the coupler to push through, i. e., the deflection of 100% corresponds to the maximum load torque. The variation

of attraction force when the magnets are shifted against each other across the magnetic field lines is non-linear in general, but for planar magnets (when the distance between the poles is less or equal to the pole width) is close to linear for about a half of the pole width (50 %). The difference between the actual and the approximated curve is clearly visible in Fig. 9, however, the third-order polynomial is extremely easy to work with, while the stiffness error magnitude is not crucial for possible applications and for the study. The choice of the polynomial coefficients may be changed on the real prototype.

Deflections higher than 50 % cannot be used effectively as the coupler enters a state of fluidity, when small variations of load torque lead to significant rotation of the rotor. It can be seen that the effective torque of the coupler is about 90 % of the push-through torque. The plot is printed for the magnets with ratio  $\frac{l}{d} = 0.5$ . Flatter magnets have a wider linear region. However, these magnets are also more sensitive to insubstantial fluctuations of the air gap that bring about undesirable torque ripple at the joint output.

The coupler output torque is inversely proportional to the cubic distance between the equivalent solenoids, which, in turn, is the sum of the magnet height and the air gap. Thus, the lesser the air gap is in comparison to magnet height, the wider operation range is allowed, but a higher manufacturing quality is required.

## Mathematical model

The calculation of the output torque  $\tau$  is based on the similarity of the family of the curves corresponding to the different air gap values. The similarity is expressed as follows:

$$\tau = \bar{\tau} \cdot \tau_{\max}, \quad (6)$$

where  $\bar{\tau}$  is the equivalent torque and  $\tau_{\max}$  is maximum torque for a given air gap acting as scale factor.

The equivalent torque depends on the equivalent deflection by a cubic polynomial:

$$\bar{\tau} = a\bar{\varphi}^3 + b\bar{\varphi}^2 + c\bar{\varphi} + d, \quad (7)$$

where the equivalent deflection reflects the multipolarity of the coupler and is defined as

$$\bar{\varphi} = \frac{n}{2\pi}\varphi, \quad (8)$$

where  $n$  is the number of the poles and  $\varphi$  is the actual deflection of the joint.

The maximum torque depends on the air gap value as follows:

$$\tau_{\max} = \frac{K}{(A + \Delta)^3}, \quad (9)$$

where  $K$  is the proportional coefficient,  $A$  is the initial (minimal) air gap, and  $\Delta$  is additional air gap.

The stiffness of any elastic object is just the first derivative of the load force or torque:

$$S = \frac{\partial \tau}{\partial \varphi}. \quad (10)$$

Then the output stiffness of the coupler and also of the joint can be found as

$$S = \tau_{\max} \cdot (3a\bar{\varphi}^2 + 2b\bar{\varphi} + c) \cdot \frac{n}{2\pi}. \quad (11)$$

## The design of the joint

A laboratory prototype of the VSA joint based on a magnetic coupler (VSA-MC) as a variable spring is designed in a modular way for a testing purpose. The modular structure is shown in Fig. 10, the notation is given in the bottom part of the figure. The joint has a serial layout whose disadvantage lies in the fact that the magnetic coupler is separated from the prismatic motion unit. Also, the latter is driven by the drive D2 with the motor of excessive power for the task. It is only justified by the application of uniform drive units. The design structure of the magnetic coupler with the PMU is shown in Fig. 11.

The design structure is as follows. Permanent NdFe-magnets are placed onto the stator (2) and the rotor (3) of the coupler. The adjustment screw (7) is rotated by the motor D2, while the buttress thread nut (8), which is engaged with the adjustment screw, is capable of prismatic motion along its guides.

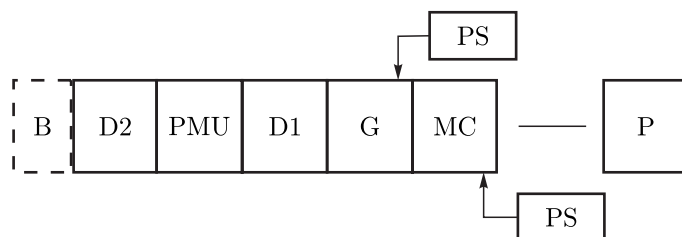


Figure 10. Modular structure of the VSA-MC. D1 and D2 – drive units, PS – position sensor, PMU – prismatic motion unit that moves the magnetic coupler, MC – magnetic coupler itself, P – plant, G – gearbox unit, B – brake unit

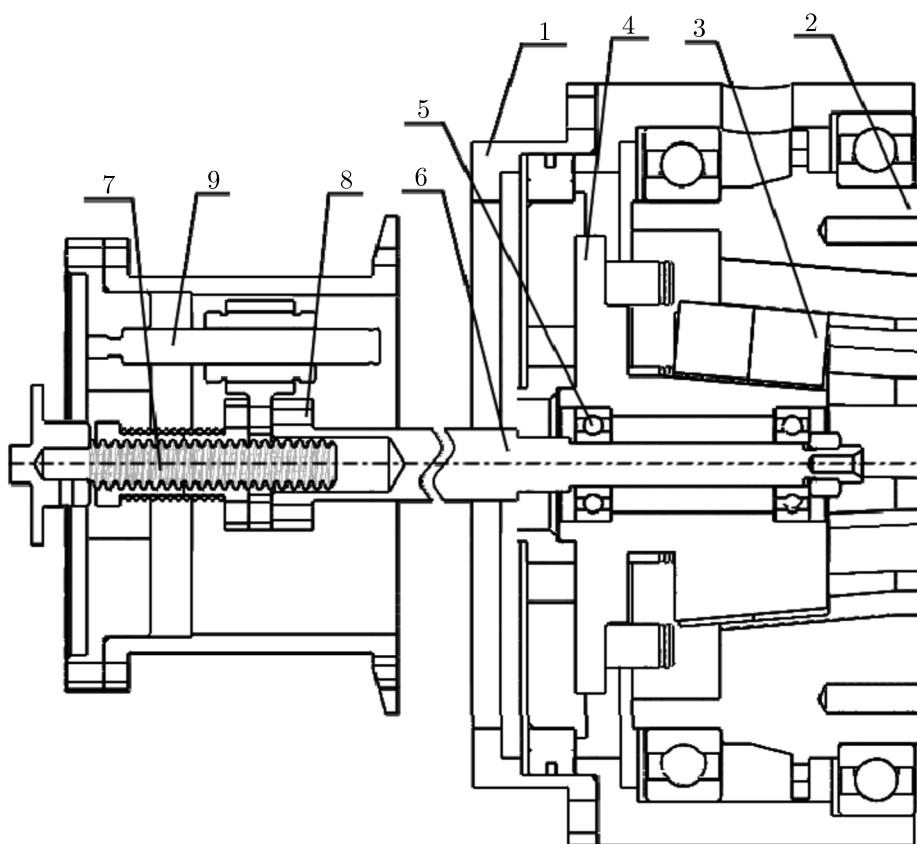


Figure 11. Design structure of the magnetic coupler with the PMU. 1 – hull, 2 – stator, 3 – rotor, 4 – rotor hub, 5 – hub bearings, 6 – adjustment pushrod, 7 – adjustment screw, 8 – buttress thread nut, 9 – guiding nuts

The nut is fixed with the pushrod (6) that pushes the rotor hub (4), into which the rotor magnets (3) are installed. The rotor hub is connected with the gearbox unit by the slide-fitted register pins, which provides the torque transmission to the rotor while allowing its transition along the axis. The transition of the rotor changes the air gap between rotor and stator magnets, which in turn changes the absolute value of magnetic force between them. The rotation of the rotor causes a restoring force that is proportional to the attractive force between the rotor and stator poles and roughly proportional to the rotation angle for small values of the angle (less than half of the pole width). Therefore, the air gap variation is equivalent to stiffness adjustment.

The main drive unit is used to adjust stiffness in this joint which is not optimal in terms of size and weight but reduces the cost of design and manufacturing of the testing prototype which is preferable for early laboratory research.

The outlook and the arrangement of the VSA-MC are presented in Fig. 12. The rotor and the stator are made as conical rings thus the air gap can be varied by transition despite the radial arrangement. The distinctive feature of the joint is operation within one angular step of magnet pole placement. If the load torque exceeds the limit the mechanism pushes through, i. e., it works as safety coupling, preventing mechanical damage to high degree. The design specification of the joint is given in Table 1.

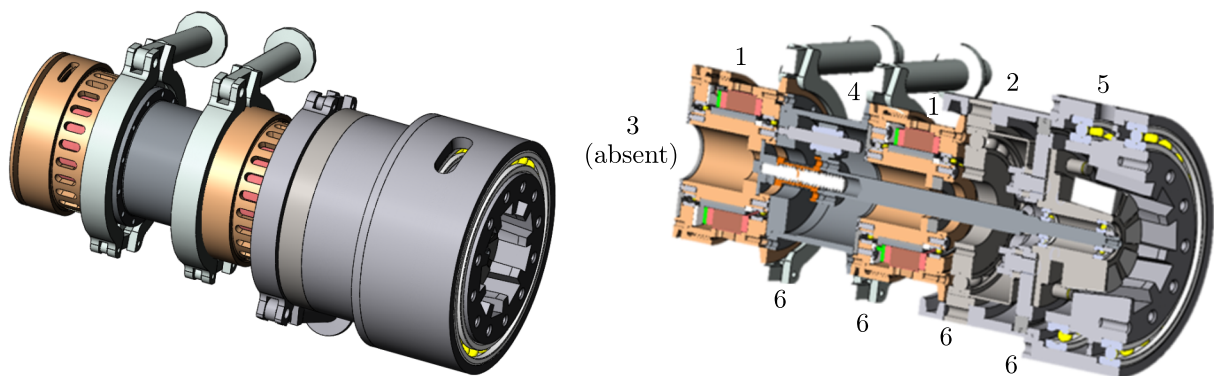


Figure 12. CAD-model of the VSA-MC: joint outlook and arrangement. 1 – drive unit, 2 – gearbox unit, 3 – brake unit (optional, not shown), 4 – prismatic motion unit, 5 – magnetic coupler, 6 – clamp

Table 1. Design specification of VSA-MC

Quantity, dimension	Value
Rated torque, Nm	100
Nominal speed, rpm	20
Power consumption, W	450
Operation range, deg	infinite
Stiffness range, Nm/rad	100 : 1000
Positioning error, ang. min	10
Dimensions, diameter × length, mm	130 × 280
Mass	8.7

## Controller design

The plant to control is described by the following equation system

$$\begin{cases} M\ddot{q} = K(\theta - q, \sigma) - g(q), \\ B\ddot{\theta} + K(\theta - q, \sigma) = \tau_m, \end{cases} \quad (12)$$

where  $M$  is the load inertia,  $K(\varphi, \sigma)$  is the elastic torque that depends on deflection  $\varphi$  and stiffness setting parameter  $\sigma$ ,  $\theta$  and  $q$  are the motor position and the link position respectively,  $g(q)$  is the gravity torque,  $B$  is the motor inertia, and  $\tau_m$  is the motor torque. The elastic torque for VSA-MC specifically can be found by expressions (6)–(9).

The first and second equations correspond to the link-side subsystem and the motor-side subsystem. The structure of VSA (12) represents an underactuated mechanical system in which only the generalized motor coordinate  $\theta$  can be directly actuated via the control input  $\tau_m$ . The generalized link coordinate  $q$  can only be indirectly actuated via the generalized elastic torque  $K(\varphi, \sigma)$ . The elastic potential depends on the additional variable  $\sigma$ , which can be considered as an input to change the characteristic of the stiffness.

The control system design for VSAs naturally stems from the control of SEAs, so the main approaches are the same, which are feedback linearization (FBL), singular perturbation approach (SPA) and passivity-based control (PBC), which is a special case of energy-shaping control. Feedback linearization was thoroughly studied by De Luca in [Palli, Melchiorri, De Luca, 2008; Buondonno, De Luca, 2016] while many different passivity-based methods were developed in DLR [Albu-Schäffer et al., 2010; Petit, Albu-Schäffer, 2011; Keppler et al., 2016]. An overall analysis of energy-shaping control is given in [Albu-Schäffer, Petit, 2012]. An example of the SPA-based method was proposed by Melchiorri [Palli, Melchiorri, 2011]. As a rule, the control of serial chain manipulators is considered that can be easily applied to the single-joint case, but still some specifically study single-joint control [Sardellitti et al., 2012; Psomopoulou et al., 2012; Sardellitti et al., 2013]. In a number of articles authors use simple PID or PI-controllers with different extensions [Sardellitti et al., 2012; Yang et al., 2022]. Not many articles are found that summarize the field, but a survey of several methods is given in [Petit, Dietrich, Albu-Schäffer, 2015] as well as in [Petit, 2014] and a comparison of two widespread approaches can be found in [Erler et al., 2014]. Examples of other approaches can be found, such as backstepping control [Petit, Daasch, Albu-Schäffer, 2015], feedforward control based on a chain of exponential filters [Biagiotti, Moriello, Melchiorri, 2017]. A widespread solution to achieve robustness is the use of a disturbance observer [Guo, Tian, Liu, 2018; Guo et al., 2019; Guo, 2020]. A combination of the feedback linearization, disturbance observer, sliding mode control and adaptive input saturation compensation law is proposed in [Guo, Tian, 2020]. A lot of attention is given to the optimal control problem [Haddadin et al., 2011; Ji, Kong, Li, 2019], but it goes beyond the scope of this work. The most practical methods were incorporated into a special ROS-toolbox [Mengacci et al., 2021].

The articles mentioned in the previous paragraph mainly considered position control. However, force-torque control and impedance control as its special case are also of interest because VSA joints are often used in contact tasks. To date there, has been a large body of research on this topic, which can be classified in the same way as position control research. The representative examples are closed-loop control [Ghorbani, Wu, 2006], adaptive impedance control [Ozawa, Kobayashi, Ishibashi, 2015], and robust cascade gain-scheduled controller [Misgeld et al., 2017]. A comparison of passivity-based impedance controllers is given in [Lendermann et al., 2015].

Of all the methods presented above the passivity-based approach has a number of important advantages: passivity guarantees stability, while there is little dependence on the joint model in the controller. This is especially explicitly expressed in the approach from [Keppler et al., 2016] which was later developed in [Keppler et al., 2018a] and named ESP, which means “elastic structure preserving” and its main idea lies in slight transformation of the plant in order to introduce virtual damping, as natural damping is usually small in such systems. The inertia and stiffness of the plant are kept natural, so to introduce damping a change of variable should be made, which is the main motor position (after the gearbox). An illustration of the approach is presented in Fig. 13.

In this article the controller [Keppler et al., 2016] is implemented with necessary simplifications. The main steps are presented below to give an overall concept. At first, let us consider a regulation

case, when only the goal position is specified and not the trajectory that the joint should follow to reach this position. With a new equivalent motor position  $\eta$  the closed-loop equation system of the plant can be written as

$$\begin{cases} M\ddot{q} = K(\eta - q, \sigma) - D\dot{q}, \\ B\ddot{\eta} + K(\eta - q, \sigma) = \bar{u}, \end{cases} \quad (13)$$

where  $D$  is the virtual damping value. By comparison of (12) and (13) a relation between the original and the new motor variable can be found:

$$K(\theta - q, \sigma) - g(q) = K(\eta - q, \sigma) - D\dot{q}. \quad (14)$$

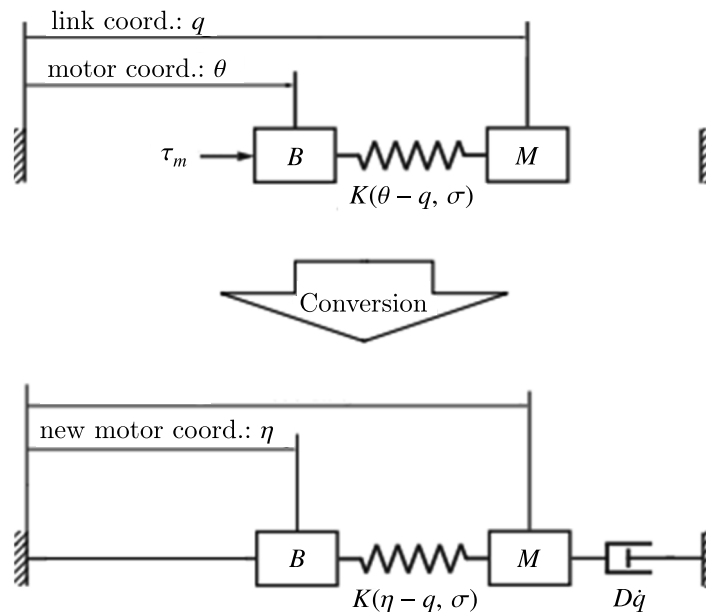


Figure 13. Original and equivalent models of the plant VSA.  $B$  – rotor inertia,  $M$  – link inertia,  $\sigma$  – stiffness adjustment parameter,  $K = K(\varphi, \sigma)$  describes the elastic behavior of the spring,  $D$  – virtual damping factor

From here,  $\eta$  is to be found and thus the inverse of  $K$  is required. The latter is usually not analytically available, so  $\eta$  has to be determined numerically. Continuing with extraction of  $\dot{\eta}$  and  $\ddot{\eta}$  from the first and second derivatives of (14), the motor acceleration can be expressed as

$$\ddot{\theta} = \ddot{q} + \psi_1^{-1} \left( -\psi_1(\dot{\theta} - \dot{q}) + \psi_2(\dot{\eta} - \dot{q}) + \psi_2(\ddot{\eta} - \ddot{q}) - \frac{d^2(D\dot{q})}{dt^2} \right) + \ddot{g}, \quad (15)$$

where  $\psi$  is the derivative of  $K$  with respect to deflection, subscripts 1 and 2 mean deflection in the original and equivalent variables, respectively. Substituting (15) into the motor-side equation of the original system (12) yields the following equation:

$$B\ddot{\eta} + B \left( \psi_1^{-1} \left( -\psi_1(\dot{\theta} - \dot{q}) + \psi_2(\dot{\eta} - \dot{q}) + \psi_2(\ddot{\eta} - \ddot{q}) - \frac{d^2(D\dot{q})}{dt^2} \right) + \ddot{g} \right) + K(\eta - q, \sigma) - D\dot{q} + g = \tau_m. \quad (16)$$

Considering the resulting equation, there are three steps to build the controller, such that

$$\tau_m = \widehat{u} + \widetilde{u}(\widehat{u}), \quad (17)$$

where  $\widehat{u}$  precompensates undesired nonlinear terms,  $\widetilde{u}$  scales the motor inertia to the original one and  $\bar{u}$  represents the PD-controller for the closed-loop plant (13), as it is proven in [Keppler et al., 2016] that it stabilizes the system if its parameters  $K_p$  and  $K_D$  are positive.

$$\widehat{u} = B\ddot{\eta} + B\left(\psi_1^{-1}\left(-\dot{\psi}_1(\dot{\theta} - \dot{q}) + \dot{\psi}_2(\dot{\eta} - \dot{q}) + \psi_2(\ddot{\eta} - \ddot{q}) - \frac{d^2(D\dot{q})}{dt^2}\right) + \ddot{g}\right) - D\dot{q} + g, \quad (18)$$

$$\widetilde{u} = (I - \psi_1^{-1}\psi_2)K(\eta - q, \sigma) + \psi_1^{-1}\psi_2\bar{u}, \quad (19)$$

$$\bar{u} = -K_p(\eta - \eta_d) - K_D\dot{\eta}. \quad (20)$$

The trajectory tracking case is very similar, only now the desired closed-loop dynamics are

$$\begin{cases} M\ddot{\bar{q}} = K(\eta - \bar{q}, \sigma) - D\dot{\bar{q}}, \\ B\ddot{\eta} + K(\eta - \bar{q}, \sigma) = \bar{u}, \end{cases} \quad (21)$$

where  $\bar{q} = q - q_d(t)$  is the tracking error. Then an additional term  $n_0$  appears in (14) on the right and with negative sign, which is

$$n_0(q, \dot{q}, t) \equiv M(q)\ddot{q}_d(t). \quad (22)$$

Repeating the same logic,  $n_1$  and then  $n_2$  can be found by taking derivatives as

$$n_1(q, \dot{q}, \ddot{q}, t) \equiv \dot{M}(q)\ddot{q}_d(t) + M(q)\dddot{q}_d(t), \quad (23)$$

$$n_2(q, \dot{q}, \ddot{q}, \ddot{\ddot{q}}, t) \equiv \ddot{M}(q)\ddot{q}_d(t) + 2\dot{M}(q)\ddot{\ddot{q}}_d(t) + M(q)q_d^{(4)}(t). \quad (24)$$

However, the control terms (19) and (20) remain the same and only the first control term changes into

$$\widehat{u} = B\ddot{\eta} + B\left(\psi_1^{-1}\left(-\dot{\psi}_1(\dot{\theta} - \dot{q}) + \dot{\psi}_2(\dot{\eta} - \dot{q}) - \psi_2\ddot{q} - \frac{d^2(D\dot{q})}{dt^2}\right) + \ddot{g} + n_2\right) - D\dot{q} + g + n_0. \quad (25)$$

Many VSA joints represent a serious issue regarding variable stiffness which is often nonlinear for any position of the adjustment drive. However, as mentioned earlier, the stiffness of VSA-MC is almost linear in a significant part of the possible deflection. Also, the parameters of the magnetic coupler can be identified with high accuracy and the operating conditions do not influence them much, so the actual stiffness value can be found from the model at any time instant with reasonable accuracy. If the stiffness can be considered known and roughly constant and thus its derivatives can be cancelled, then the equations become much easier and the controller can be designed as in [Shardyko, Samorodova, Titov, 2020; Samorodova, Igor, Titov, 2020].

The next issue is to tune the controller. The authors in [Keppler et al., 2016] suggest a critical damping approach, however, the system cannot be divided exactly into two second-order subsystems. In [Shardyko, Samorodova, Titov, 2021] it was shown that the positive torque feedback actually decouples the system in this way at the cost of stability deterioration. A simple tuning procedure was proposed in [Shardyko, Samorodova, Titov, 2020], leaving three tuning parameters, proportional coefficient  $K_P$  and two damping ratios, for motor-side and link-side, respectively. As the elastic properties are determined entirely by the plant stiffness, the proportional coefficient should be made as large as possible while avoiding saturation and keeping the system stable considering implementation issues such as discretization and non-linearities of the plant. Damping ratios should be chosen to achieve some compromise between the transient time and the overshoot. All the controller gains can then be found in a straightforward way as

$$K_D = 2\gamma\sqrt{B(K_P + K)}, \quad (26)$$

$$D = 2\gamma\sqrt{MK}. \quad (27)$$

A more complex analysis is given by investigating the whole 4th order polynomial in [Dalyaev et al., 2020], but usually a simple procedure is enough.

However, what we have is not a simple SEA-joint, but a VSA-joint, so additionally a mechanical stiffness control command is required, and in a general way both commands have to be performed at the same time. Simultaneous trajectory and stiffness control can be nontrivial for some types of VSA joints, but it is rather straightforward for VSA-MC due to the nonbackdrivability of the ball-screw transmission and the moderate nonlinearity of the magnetic spring itself. If some value of stiffness  $S_d$  is desired, it should be first found what should be the air gap value  $\Delta_d$  using (6)–(10). Next, the desired rotation angle of the adjustment motor can be found simply as

$$\sigma_d = \Delta_d r_\sigma, \quad (28)$$

where  $r_\sigma$  is the appropriate transmission ratio.

The equation of stiffness adjustment motor system neglecting friction can be written simply as

$$B_\sigma \ddot{\sigma} = \tau_\sigma, \quad (29)$$

where  $B_\sigma$  is the rotor inertia of the adjustment motor and  $\tau_\sigma$  is the adjustment motor torque.

A traditional PD-controller can be applied to this system, and for a standard damped second-order equation the controller gains should be set as follows:

$$K_{P\sigma} = \frac{B_\sigma}{T^2}, \quad (30)$$

$$K_{D\sigma} = 2\gamma_\sigma T K_{P\sigma}, \quad (31)$$

where  $T$  is the time constant and  $\gamma_\sigma$  is the damping ratio.

The controller should be fast enough to comply with the stiffness variation speed caused by deflection. As stated above, the nonlinearity of this relationship is weak, so even quite a slow motor can be applied.

The trajectory tracking controller designed earlier makes the system execute the trajectory as accurately as possible regardless of the external forces. In this way, natural joint elasticity can only reduce external impact at the initial phase but in many tasks it is required that the joint should interact with external objects with specific stiffness, which is called virtual stiffness. Such tasks typically involve impedance control techniques introduced by Hogan [Hogan, 1985]. A detailed review on impedance control history and application can be found in [Shardyko, Kopylov, Titov, 2022]. In DLR, after the development of ESP control the same principle of introduction the equivalent motor variable was applied to impedance control as ES $\pi$  approach (elastic structure preserving impedance control) [Keppler et al., 2018b], which is shown in Fig. 14. This approach keeps all the advantages of ESP control and therefore is suitable to implementation in VSA-MC.

The desired dynamics in this case can be described in the general trajectory tracking case as

$$\begin{cases} M(q)\ddot{q} = K(\eta - \bar{q}, \sigma) - D_q \dot{q} - K_q \bar{q}, \\ B\ddot{\eta} + K(\eta - \bar{q}, \sigma) = D_\eta \dot{\eta}. \end{cases} \quad (32)$$

In the regulation case (32) simplifies to

$$\begin{cases} M(q)\ddot{q} = K(\eta - q, \sigma) - D_q \dot{q} - K_q(q - q_d), \\ B\ddot{\eta} + K(\eta - q, \sigma) = D_\eta \dot{\eta}. \end{cases} \quad (33)$$

If the stiffness can be considered known and slowly changing, then the elastic torque is simply

$$K(\eta - q, \sigma) = K_e(\eta - q). \quad (34)$$

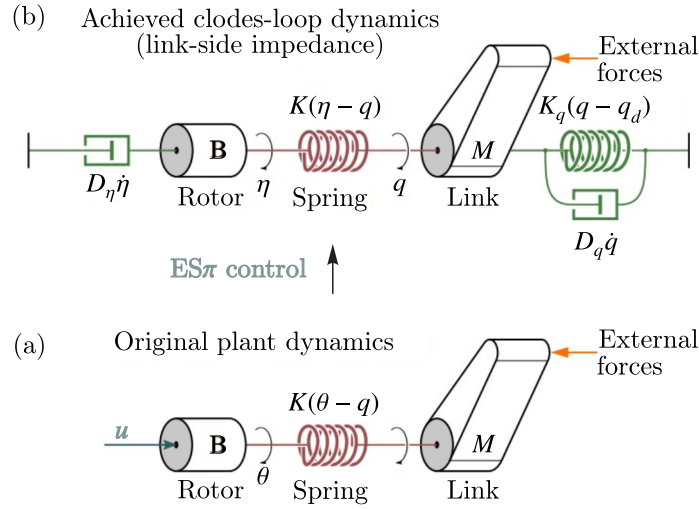


Figure 14. Visual representation of the model transformation for ES $\pi$  approach [Keppler et al., 2018b].  $B$  – rotor inertia,  $M$  – link inertia,  $K$  – spring stiffness,  $D_\eta$  – controller parameter,  $\theta$  and  $\eta$  – actual and equivalent motor position,  $q$  – link position,  $K_q$  and  $D_q$  – virtual stiffness and damping

After the appropriate transformations and substitutions, the motor control torque for the regulation case takes the form

$$\tau_m = -K_d \dot{\eta} - K_D \dot{q} - K_P(q - q_d) - BK^{-1}K_D \ddot{q} - BK^{-1}K_P \ddot{q}, \quad (35)$$

with

$$\eta = \theta + K^{-1}(K_D \dot{q} + K_P(q - q_d)). \quad (36)$$

In the trajectory tracking case the motor control torque is

$$\tau_m = -K_d \dot{\eta} + B \ddot{q}_d + BK_e^{-1} \ddot{n} - BK_e^{-1} K_D (\ddot{q} - \ddot{q}_d) - BK_e^{-1} K_P (\ddot{q} - \ddot{q}_d) + M \ddot{q}_d - K_D (\dot{q} - \dot{q}_d) - K_P (q - q_d) \quad (37)$$

with

$$\eta = \theta - q_d - K_e^{-1} M \ddot{q}_d + K_e^{-1} K_D (\dot{q} - \dot{q}_d) + K_e^{-1} K_P (q - q_d). \quad (38)$$

Both controllers, as can be seen from equations (18) and (37), contain higher (second and third) derivatives of the output joint position, which may seem suspicious. However, in previous works [Keppler et al., 2016; Samorodova, Igor, Titov, 2020] it was shown that terms with higher derivatives can be neglected without any significant loss of performance for the position control case. For the impedance control case the performance is even less crucial with respect to stability so again, it seems possible to neglect the higher derivatives terms. Thereby, respective terms of the controllers are dropped in the simulation below. A thorough analysis is planned to be conducted in the future work including hardware tests.

## Simulation tests

In order to confirm the workability and to study the performance of the control algorithms presented above, a series of simulation tests have been carried out for the continuous-time system. Discretization effects were not taken into account, which is partly justified by the slow nature of the elastic joint. This influence is expected to be investigated along with other implementation issues on a real prototype in future work. The first group of tasks considered the case without external load and contained step and trajectory tasks with noncontrolled specified air gap value, and thus stiffness, as well as a task of simultaneous trajectory and stiffness control. Note that the stiffness value itself

was not regulated, just the air gap value, and the goal is to check the position trajectory controller. Variable stiffness can be interpreted as a model variation here, while actual simultaneous position and stiffness control is an issue for the future and a novel controller should be designed in this respect. The following control algorithms were tested: (17) with (18) for the position step task, (17) with (25) for the position trajectory task, and finally (17) with (25) and (30)–(31) for the simultaneous position and stiffness trajectory task. The results are presented in Fig. 15, Fig. 16 and Fig. 17, respectively. The step task command is  $\frac{\pi}{18}$  rad, which is also the total rotation angle for the trajectory task. The trajectory is chosen as a 5<sup>th</sup> order polynomial that is to be performed in 1 sec starting at 0.05 sec. Control parameters are chosen as follows:  $K_p = 10,000$ ,  $\gamma_1 = \gamma_2 = 1$ . Stiffness is controlled indirectly by regulating the air gap value, and the following control parameters are chosen:  $\gamma_\sigma = 1$ ,  $K_\sigma$  is shown in Fig. 17.

Different plots in Fig. 15 and Fig. 16 correspond to different stiffness presets, which are 7 in total: constant air gap from 0 % to 100 % of the allowable range and two variable air gap presets, where the air gap changes from minimum to maximum and vice versa, during the first second of the task. In the trajectory tracking case the task is also given for a first second. The results show that the system is stable and shows zero overshoot for the whole range of stiffness variation. The transient rate of step tasks depends on the specific mechanical stiffness as well as the trajectory tracking error. The variation of mechanical stiffness changes performance instantly.

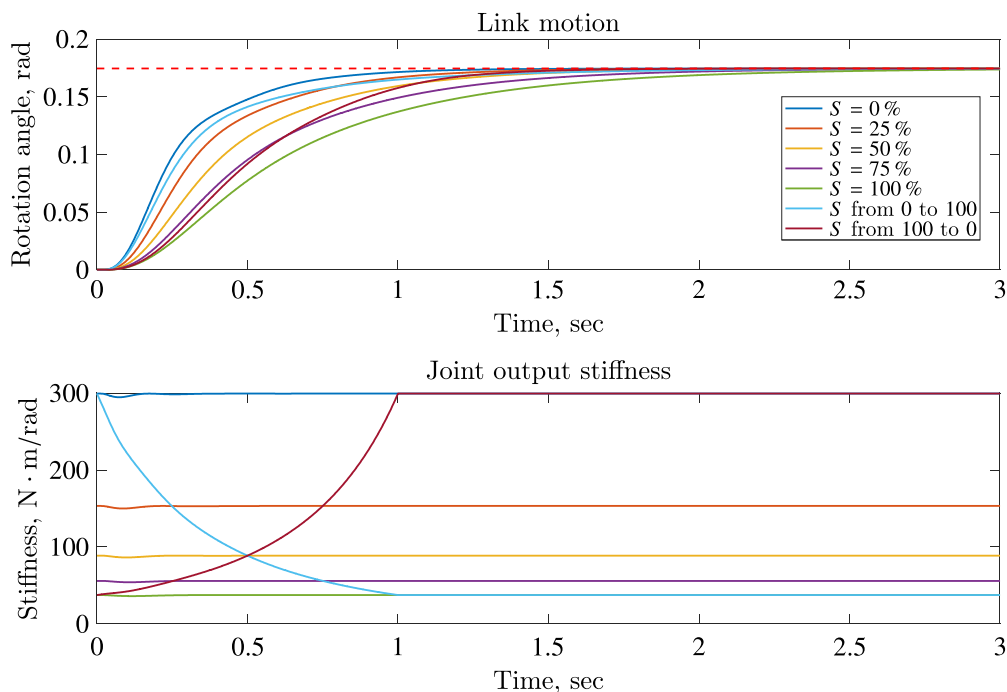


Figure 15. Step task performance with specified air gap in the magnetic coupler.  $S$  is the air gap level with 0 and 100 being the minimum and maximum levels, respectively. The step command is  $\frac{\pi}{18}$  rad = 0.1745 (dashed line). Control parameters are:  $K_p = 10,000$ ,  $\gamma_1 = \gamma_2 = 1$

When the trajectory and stiffness are controlled simultaneously, the trajectory performance is similar to the previous case, but there are issues with stiffness control. As the motor-gearbox unit has a certain time response, the stiffness variation speed is limited by it. This is clearly visible in plots. The stiffness task is a half-period of a sine function with a period of 4 seconds, with a constant offset of 50 N · m/rad. The magnitude of the sine ( $A$ ) and the time constant of the actuator ( $T$ ) are depicted in the plot legend. It is clearly visible that the lesser value of time constant works fine for a small

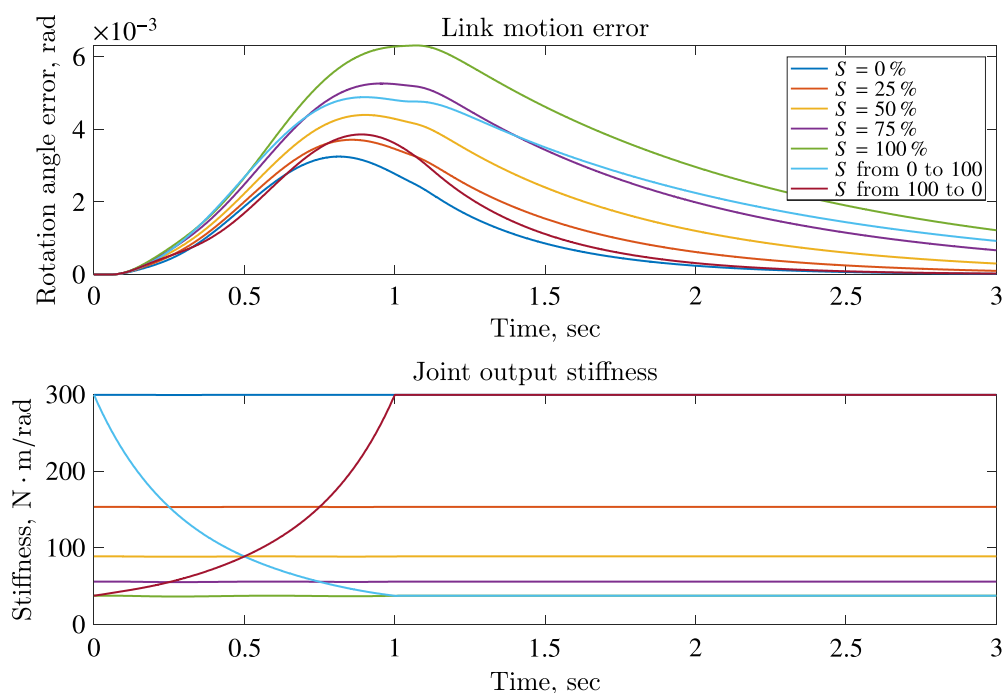


Figure 16. Trajectory tracking performance in position mode with specified air gap in the magnetic coupler.  $S$  is the air gap level with 0 and 100 being the minimum and maximum levels, respectively. The task trajectory is a 5<sup>th</sup> order polynomial to be executed in 1 sec starting at 0.05 sec. The total rotation angle is  $\frac{\pi}{18}$  rad = 0.1745. Control parameters are:  $K_p = 10,000$ ,  $\gamma_1 = \gamma_2 = 1$

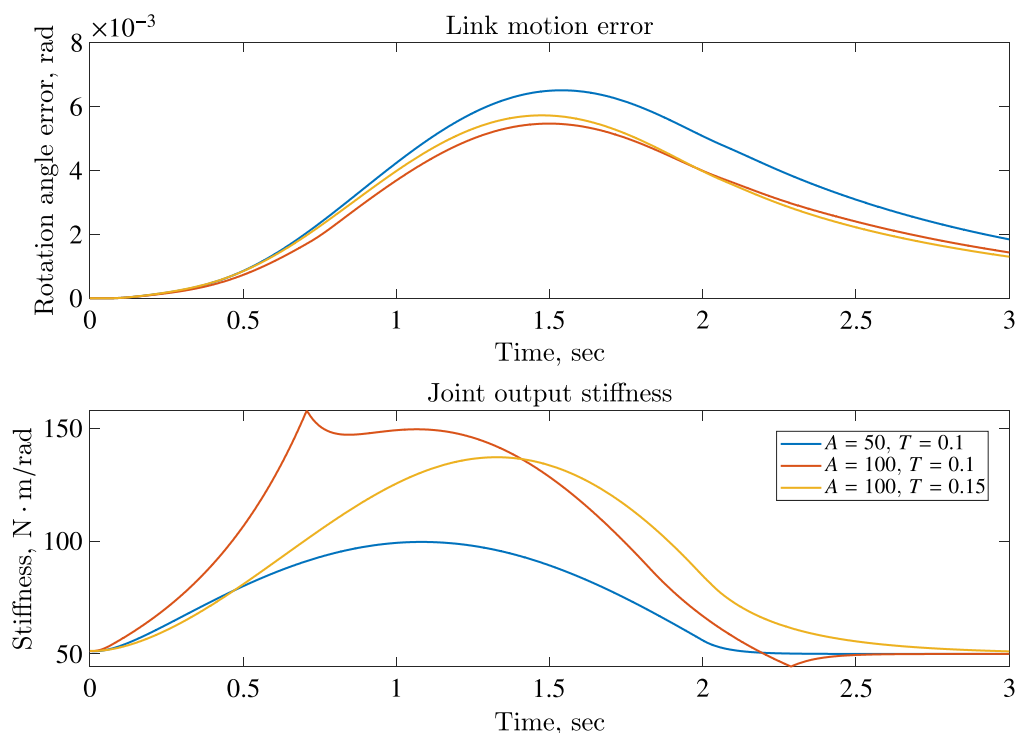


Figure 17. The performance of the simultaneous trajectory and stiffness task. Stiffness is set to follow a sine with magnitude  $A$  an time period of 4 seconds. The stiffness actuator time constant is set to  $T$ . The task trajectory is a 5<sup>th</sup> order polynomial to be executed in 1 sec starting at 0.05 sec. The total rotation angle is  $\frac{\pi}{18}$  rad = 0.1745

magnitude, but leads to saturation and nonsmooth stiffness tracking when the magnitude becomes high enough. Then, by increasing the time constant the tracking becomes smooth again but is significantly slower, which can be insufficient in a specific task. Therefore, not only the position trajectory but also the stiffness trajectory should be checked for feasibility beforehand if it is affordable.

Another important case to be considered is action against the external load, including the effect of stiffness variation. Figure 18 shows the results for two tests, with stiffness decreasing and increasing in steps. The external torque was  $10 \text{ N} \cdot \text{m}$  and  $5 \text{ N} \cdot \text{m}$ , respectively. The tests show that the effective joint stiffness with ESP controller is determined by the mechanical spring elasticity, thus the elastic structure is actually preserved.

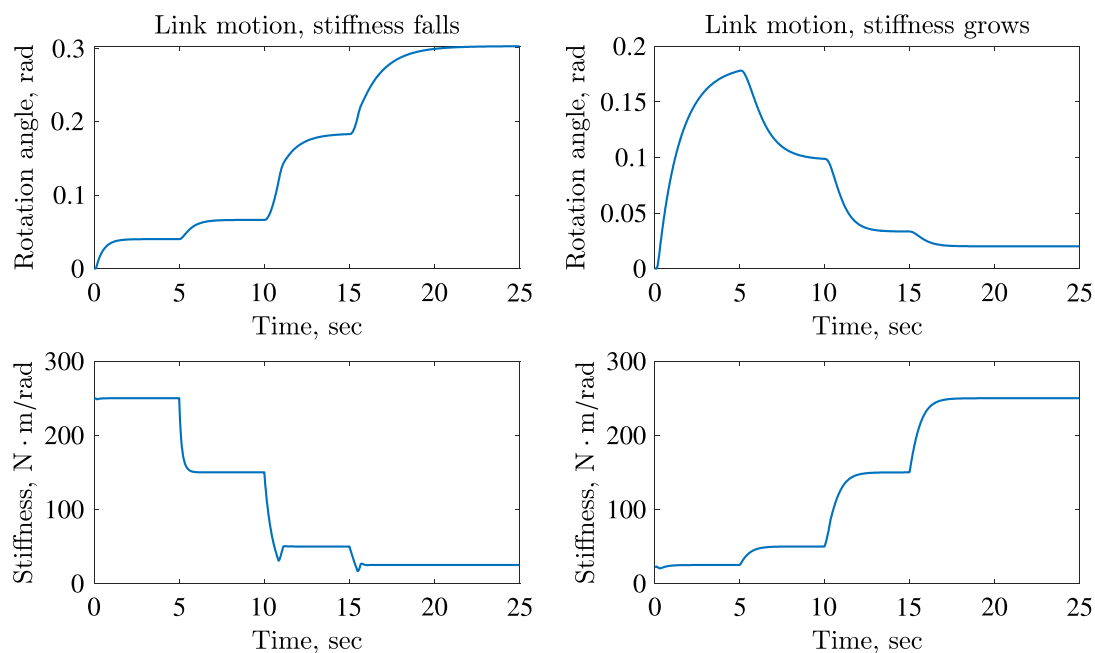


Figure 18. Joint response to external load ( $\tau_{\text{ext}} = 10 \text{ N} \cdot \text{m}$ ) with position controller. The stiffness is changed indirectly by air gap regulation (below). Transient and steady-state behavior are visible (above). The position task (rotation angle) is always 0

Next, the impedance control was studied with  $\text{ES}\pi$  controller, which was implemented as (37) for trajectory tracking as a universal case. The first test was also trajectory tracking without external load with specific stiffness settings as for the position controller earlier, and the results are shown in Fig. 19. The response is stable with no overshoot in all the tests but the oscillating nature reveals for small values of stiffness, which is likely due to the saturation of control signal when the low stiffness requires higher values of control to move the link. The oscillations, however, are moderate and don't present any critical issue.

The response to the external load is also very important because impedance control is conceived for interactions tasks. The test which is analogous to Fig. 18 was conducted with a constant value of the virtual stiffness gain  $K_p$ . The results are shown in Fig. 20 and they are quite different from the previous test where the position controller (ESP) was used. This time the steady-state deflection is independent of the mechanical stiffness because it is determined by the virtual stiffness, i. e., proportional controller gain. Nevertheless, the transient still depends on the stiffness of the magnetic coupler, and transient error grows, while stiffness decreases.

In contrast, the variable virtual stiffness was considered in the next test. The magnetic coupler stiffness task was set at  $50 \text{ N} \cdot \text{m}/\text{rad}$ . The results are shown in Fig. 21 and they demonstrate

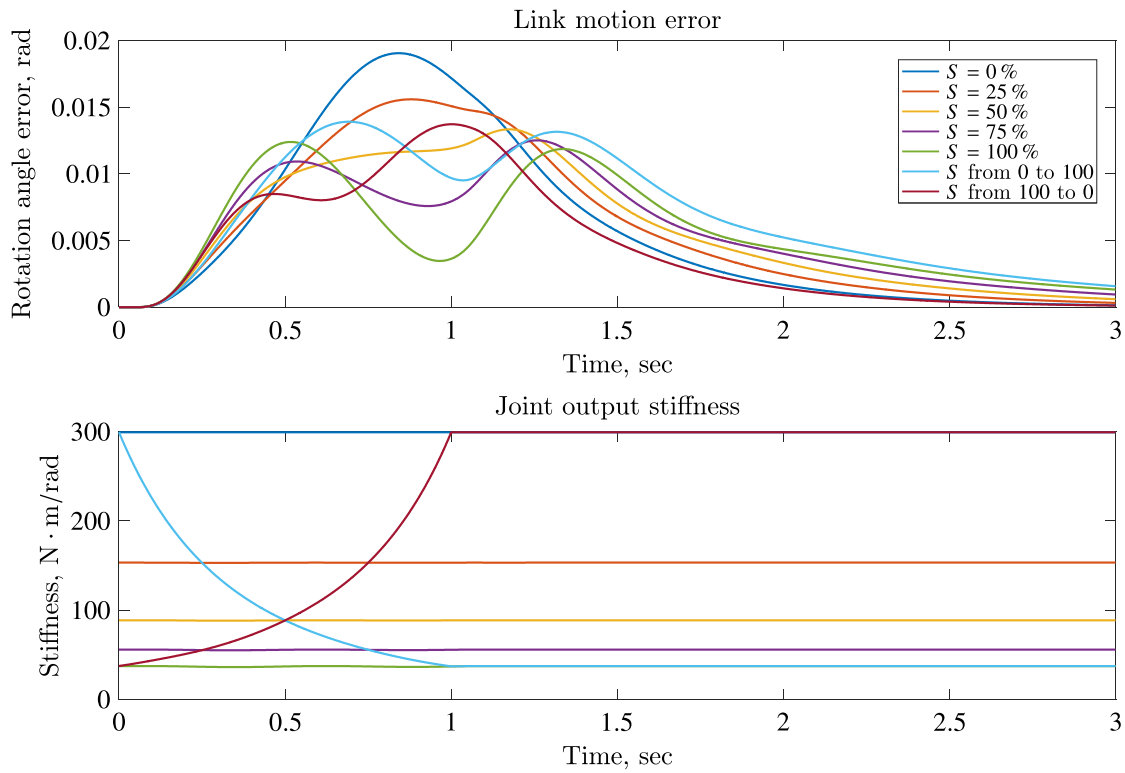


Figure 19. Trajectory tracking performance in impedance mode with specified air gap in the magnetic coupler.  $S$  is the air gap level with 0 and 100 being the minimum and maximum levels, respectively. The task trajectory is a 5<sup>th</sup> order polynomial to be executed in 1 sec starting at 0.05 sec. The total rotation angle is  $\frac{\pi}{18}$  rad

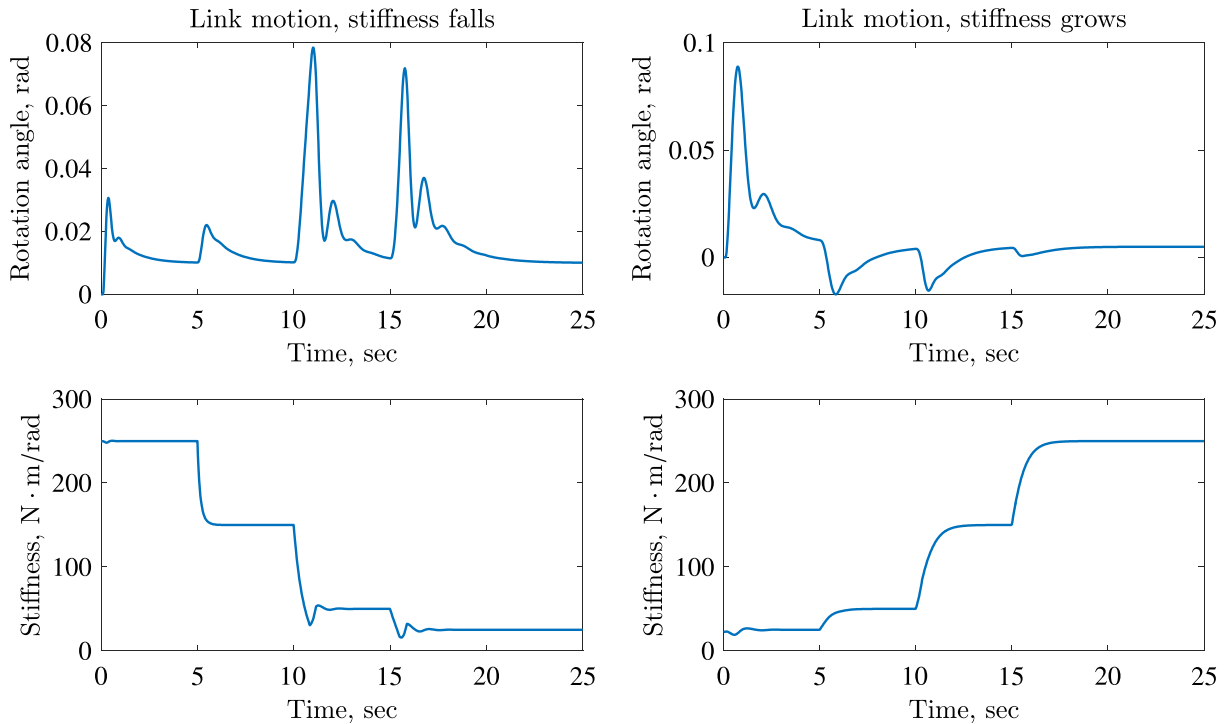


Figure 20. Joint response to external load ( $\tau_{ext} = 10 \text{ N} \cdot \text{m}$ ) with impedance controller with constant virtual stiffness. The joint mechanical stiffness is changed by open-loop control to obtain four different values (below). Transient and steady-state behavior are visible (above). The position task (rotation angle) is always 0

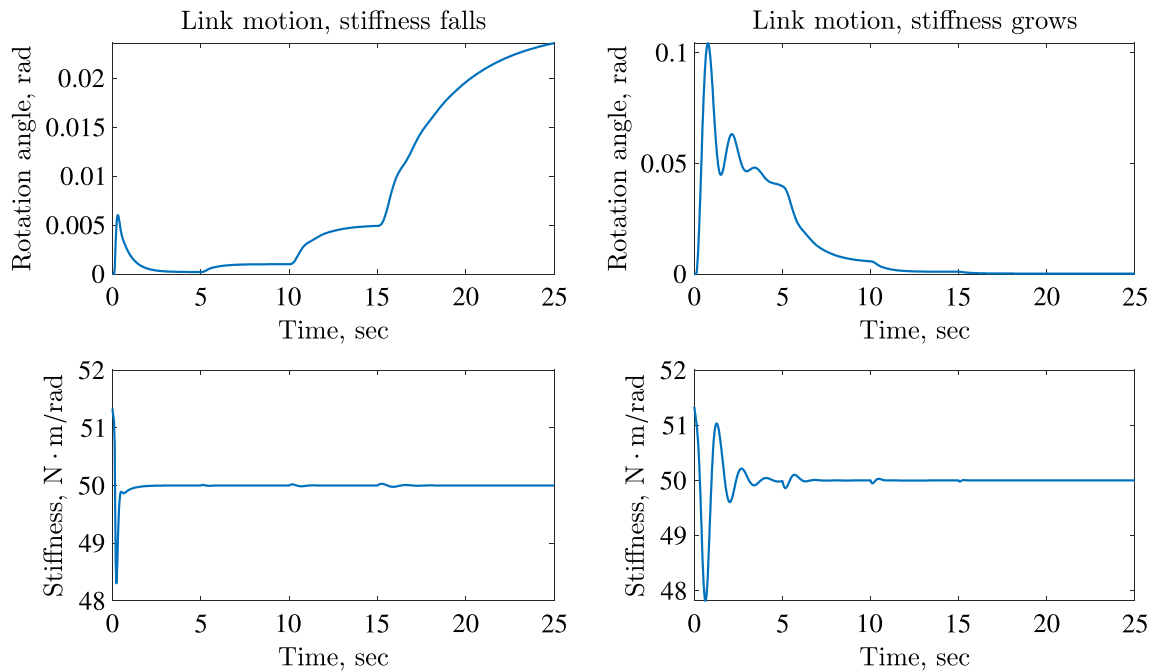


Figure 21. Joint response to external load ( $\tau_{\text{ext}} = 10 \text{ N} \cdot \text{m}$ ) with impedance controller with variable virtual stiffness and constant mechanical stiffness. The virtual stiffness is changed by impedance control to obtain four different values from the row  $\{25000, 5000, 1000, 200\}$ . Mechanical stiffness is shown below. Transient and steady-state behavior are visible (above). The position task (rotation angle) is always 0

that the joint is deflected for a different angle for every virtual stiffness setting, while the coupler stiffness was indeed kept nearly constant. The virtual stiffness setting was changed once every five seconds except the last where still the fourth setting was used. The values were chosen from the row  $\{25000, 5000, 1000, 200\} \text{ N} \cdot \text{m/rad}$  and then backwards.

The last test considers the above-mentioned stability robustness of the controller to the model parameters. As we have only one joint without friction as a plant, there are only three parameters, i. e., motor inertia, load inertia and joint stiffness. The latter is variable in the case of VSA and the robustness is difficult to test, however, the previous experiments (Figs. 15, 16, 19) in fact showed that the controller preserves stability in the whole stiffness range of the joint model. Motor inertia is given in specification, while it can also be measured with high precision and the value is constant under any working conditions, so it is pointless to check robustness to this parameter. The only parameter left is the load inertia, which cannot be identified well enough or can be changed when some payload is attached to the joint output. The following test keeps the load inertia of the model which is used in the controller  $M$ , but we change the actual model parameter from  $25M$  to  $0.04M$ . The test itself repeats the step task of Fig. 15, which is a step of  $\frac{\pi}{18}$  with  $K_p = 10,000$ , and  $\gamma_1 = \gamma_2 = 1$ . The results are shown in Fig. 22. It is clearly visible that all responses are stable though the performance deteriorates when parameter errors grow, especially when the actual inertia is larger than its model value. This is due to the fact that, according to (17), (26), and (27), the model value of inertia influences only the virtual damping, so in the worst case the system is heavily underdamped, but still stable.

## Conclusion

This paper presents a novel type of a variable stiffness actuator which has an independent layout and contains a magnetic coupler as a stiffness adjustment mechanism. The novelty is the implementation of coupler that has a conical design making it possible to change the air gap while

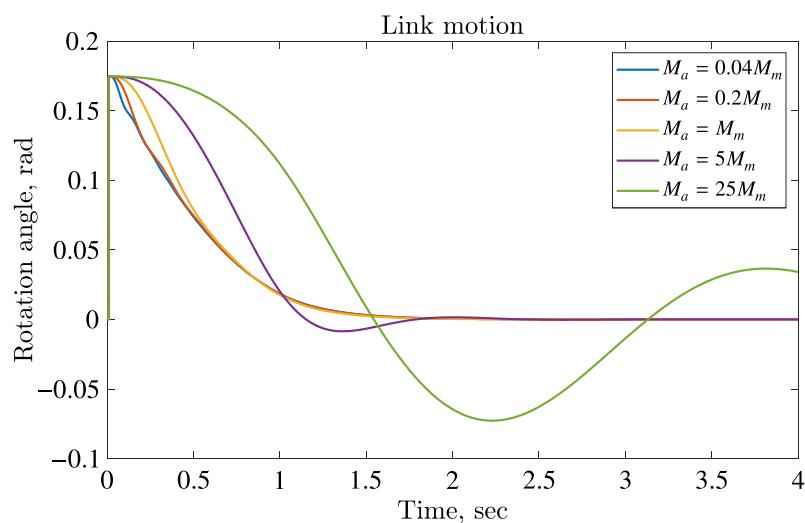


Figure 22. Results for test on robustness to load inertia  $M$ . The task is a step of  $\frac{\pi}{18}$  rad (final value is zero).  $M_a$  and  $M_m$  are the actual value and model value of the load inertia respectively

keeping concentric shape. All the necessary analyses have been performed in order to obtain the design that suits the initial requirements, the mathematical model of the joint is deduced as well. In addition, the joint follows the modular approach, the details of which are provided along with the CAD-model and the technical data.

A control system has also been investigated, and the ESP-approach, which follows the passivity-based control paradigm, was chosen to implement. The performance of the controller, as well as the behavior of the joint itself, was verified through simulation tests that considered both regulation and tracking tasks in stiff position and impedance applications. The effects of virtual and mechanical stiffness variation were compared to confirm the theoretical reasoning. The joint is in production currently, so in the future we plan to validate the joint behavior and the controller performance on the physical prototype to study the influence of hardware implementation issues such as, e. g., time discretization.

## References

- Albu-Schäffer A., Petit C. O. F.* Energy shaping control for a class of underactuated euler-lagrange systems // IFAC Proceedings Volumes. — 2012. — Vol. 45, No. 22. — P. 567–575.
- Albu-Schäffer A., Wolf S., Eiberger O., Haddadin S., Petit F., Chalon M.* Dynamic modelling and control of variable stiffness actuators // 2010 IEEE International Conference on Robotics and Automation. — IEEE, 2010. — P. 2155–2162.
- Biagiotti L., Moriello L., Melchiorri C.* Feedforward control of variable stiffness joints robots for vibrations suppression // 2017 IEEE International Conference on Robotics and Automation (ICRA). — IEEE, 2017. — P. 5289–5294.
- Buondonno G., De Luca A.* Efficient computation of inverse dynamics and feedback linearization for VSA-based robots // IEEE robotics and automation letters. — 2016. — Vol. 1, No. 2. — P. 908–915.
- Choi J., Park S., Lee W., Kang S. C.* Design of a robot joint with variable stiffness // 2008 IEEE International Conference on Robotics and Automation. — IEEE, 2008. — P. 1760–1765.
- Dalyaev I., Kopylov V., Titov V., Shardyko I.* On gain selection of active damping injection controller for series elastic actuators // 2020 International Conference Nonlinearity, Information and Robotics (NIR). — IEEE, 2020. — P. 1–6.

- Erler P., Beckerle P., Strah B., Rinderknecht S.* Experimental comparison of nonlinear motion control methods for a variable stiffness actuator // 5th IEEE RAS/EMBS International Conference on Biomedical Robotics and Biomechanics. — IEEE, 2014. — P. 1045–1050.
- Ghorbani R., Wu Q.* Closed loop control of an intentionally adjustable compliant actuator // 2006 American Control Conference. — IEEE, 2006. — P. 6.
- Guo J.* Robust tracking control of variable stiffness joint based on feedback linearization and disturbance observer with estimation error compensation // IEEE Access. — 2020. — Vol. 8. — P. 173732–173754.
- Guo Z., Sun J., Ling J., Pan Y., Xiao X.* Robust trajectory tracking control for variable stiffness actuators with model perturbations // Frontiers in Neurorobotics. — 2019. — Vol. 13. — P. 35.
- Guo J., Tian G.* Robust tracking control of the variable stiffness actuator based on the lever mechanism // Asian Journal of Control. — 2020. — Vol. 22, No. 2. — P. 729–749.
- Guo J., Tian G., Liu S.* Feedback linearization and disturbance observer based control with anti-windup for a class of variable stiffness actuators based on lever mechanisms // 2018 IEEE International Conference on Information and Automation (ICIA). — IEEE, 2018. — P. 1003–1010.
- Haddadin S., Weis M., Wolf S., Albu-Schäffer A.* Optimal control for maximizing link velocity of robotic variable stiffness joints // IFAC Proceedings Volumes. — 2011. — Vol. 44, No. 1. — P. 6863–6871.
- Ham R., Sugar T., Vanderborght B., Hollander K., Lefeber D.* Compliant actuator designs // IEEE Robotics & Automation Magazine. — 2009. — Vol. 3, No. 16. — P. 81–94.
- Hogan N.* Impedance control: an approach to manipulation, Part I — Theory, Part II — Implementation, Part III — Applications // ASME J. Dynam. Syst., Meas., Contr. — 1985. — Vol. 107. — P. 1–24.
- Hossain M. E., Bird J. Z., Albarran V., Che D.* Analysis and experimental testing of a new type of variable stiffness magnetic spring with a linear stroke length // 2021 IEEE Energy Conversion Congress and Exposition (ECCE). — IEEE, 2021. — P. 5961–5965.
- Hyun M. W., Yoo J., Hwang S. T., Choi J. H., Kang S., Kim S. J.* Optimal design of a variable stiffness joint using permanent magnets // IEEE transactions on magnetics. — 2007. — Vol. 43, No. 6. — P. 2710–2712.
- Ji C., Kong M., Li R.* Time-energy optimal trajectory planning for variable stiffness actuated robot // IEEE Access. — 2019. — Vol. 7. — P. 14366–14377.
- Keppler M., Lakatos D., Ott C., Albu-Schäffer A.* A passivity-based approach for trajectory tracking and link-side damping of compliantly actuated robots // 2016 IEEE International Conference on Robotics and Automation (ICRA). — IEEE, 2016. — P. 1079–1086.
- Keppler M., Lakatos D., Ott C., Albu-Schäffer A.* Elastic structure preserving (esp) control for compliantly actuated robots // IEEE Transactions on Robotics. — 2018a. — Vol. 34, No. 2. — P. 317–335.
- Keppler M., Lakatos D., Ott C., Albu-Schäffer A.* Elastic structure preserving impedance (ES $\pi$ ) control for compliantly actuated robots // 2018 IEEE/RSJ International Conference on Intelligent Robots and Systems (IROS). — IEEE, 2018b. — P. 5861–5868.
- Lendermann M., Singh B. R., Stuhlenmiller F., Beckerle P., Rinderknecht S., Manivannan P. V.* Comparison of passivity based impedance controllers without torque-feedback for variable stiffness actuators // 2015 IEEE International Conference on Advanced Intelligent Mechatronics (AIM). — IEEE, 2015. — P. 1126–1131.
- Liu Z., Jin H., Zhang H., Liu Y., Long Y., Liu X., Zhao J.* A variable stiffness actuator based on second-order lever mechanism and its manipulator integration // 2021 IEEE International Conference on Robotics and Automation (ICRA). — IEEE, 2021. — P. 6999–7005.
- Mengacci R., Zambella G., Grioli G., Caporale D., Catalano M. G., Bicchi A.* An open-source ROS-gazebo toolbox for simulating robots with compliant actuators // Frontiers in Robotics and AI. — 2021. — P. 246.

- Migliore S. A., Brown E. A., DeWeerth S. P. Biologically inspired joint stiffness control // Proceedings of the 2005 IEEE international conference on robotics and automation. — IEEE, 2005. — P. 4508–4513.
- Misgeld B. J. E., Hewing L., Liu L., Leonhardt S. Robust gain-scheduled control of variable stiffness actuators // IFAC-PapersOnLine. — 2017. — Vol. 50, No. 1. — P. 8804–8809.
- Olaru R., Petrescu C., Arcire A. Design of a magnetic spring for variable stiffness actuators // Proceedings of the Romanian Academy Series A. Mathematics Physics Technical Sciences Information Science. — 2021. — Vol. 22, No. 3. — P. 239–246.
- Ozawa R., Kobayashi H., Ishibashi R. Adaptive impedance control of a variable stiffness actuator // Advanced Robotics. — 2015. — Vol. 29, No. 4. — P. 273–286.
- Palli G., Melchiorri C. Output-based control of robots with variable stiffness actuation // Journal of Robotics. — 2011. — Vol. 2011.
- Palli G., Melchiorri C., De Luca A. On the feedback linearization of robots with variable joint stiffness // 2008 IEEE international conference on robotics and automation. — IEEE, 2008. — P. 1753–1759.
- Petit F. Analysis and control of variable stiffness robots. — Thesis. — ETH-Zürich, 2014.
- Petit F., Albu-Schäffer A. State feedback damping control for a multi dof variable stiffness robot arm // 2011 IEEE international conference on robotics and automation. — IEEE, 2011. — P. 5561–5567.
- Petit F., Daasch A., Albu-Schäffer A. Backstepping control of variable stiffness robots // IEEE Transactions on Control Systems Technology. — 2015. — Vol. 23, No. 6. — P. 2195–2202.
- Petit F., Dietrich A., Albu-Schäffer A. Generalizing torque control concepts: Using well-established torque control methods on variable stiffness robots // IEEE Robotics & Automation Magazine. — 2015. — Vol. 22, No. 4. — P. 37–51.
- Pirooz H. D., Eftekharian A. A., Shahri A. M., Eftekhari Yazdi M. Design and implementation of a novel two stage mechanical–magnetic variable stiffness actuator ( $M^2$ -VSA) // Advanced Robotics. — 2014. — Vol. 28, No. 24. — P. 1677–1689.
- Pratt G. A., Williamson M. M. Series elastic actuators // Proceedings 1995 IEEE/RSJ International Conference on Intelligent Robots and Systems. Human Robot Interaction and Cooperative Robots. — IEEE, 1995. — Vol. 1. — P. 399–406.
- Psomopoulou E., Doulgeri Z., Rovithakis G. A., Tsagarakis N. G. A simple controller for a variable stiffness joint with uncertain dynamics and prescribed performance guarantees // 2012 IEEE/RSJ International Conference on Intelligent Robots and Systems. — IEEE, 2012. — P. 5071–5076.
- Pyatin Yu. M. (ed.) Postoyannye magnity: spravochnik [Permanent magnets: handbook]. — Moscow: Energiya, 1980 (in Russian).
- Samorodova M., Igor S., Titov V. Control system of manipulator with elastic joints based on regulator with active damping // Extreme Robotics. — 2020. — Vol. 1. — P. 146–154.
- Sardellitti I., Medrano-Cerda G., Tsagarakis N. G., Jafari A., Caldwell D. G. A position and stiffness control strategy for variable stiffness actuators // 2012 IEEE International Conference on Robotics and Automation. — IEEE, 2012. — P. 2785–2791.
- Sardellitti I., Medrano-Cerda G. A., Tsagarakis N., Jafari A., Caldwell D. G. Gain scheduling control for a class of variable stiffness actuators based on lever mechanisms // IEEE Transactions on Robotics. — 2013. — Vol. 29, No. 3. — P. 791–798.
- Shardyko I., Kopylov V., Titov V. Impedance control of an elastic actuator with strongly coupled structure // Interactive Collaborative Robotics: 7th International Conference, ICR 2022, Fuzhou, China, December 16–18, 2022, Proceedings. — Cham: Springer International Publishing, 2022. — P. 117–129.

- Shardyko I., Samorodova M., Titov V.* Development of control system for a SEA-joint based on active damping injection // 2020 International Conference on Industrial Engineering, Applications and Manufacturing (ICIEAM). — IEEE, 2020. — P. 1–6.
- Shardyko I., Samorodova M., Titov V.* Series elastic actuator control based on active damping injection with positive torque feedback // 2021 International Conference on Industrial Engineering, Applications and Manufacturing (ICIEAM). — IEEE, 2021. — P. 613–618.
- Sun Y., Tang P., Dong D., Zheng J., Chen X., Bai L.* Modeling and experimental evaluation of a pneumatic variable stiffness actuator // IEEE/ASME Transactions on Mechatronics. — 2021. — Vol. 27, No. 5. — P. 2462–2473.
- Tonietti G., Schiavi R., Bicchi A.* Design and control of a variable stiffness actuator for safe and fast physical human/robot interaction // Proceedings of the 2005 IEEE international conference on robotics and automation. — IEEE, 2005. — P. 526–531.
- Vanderborght B., Albu-Schäffer A., Bicchi A., Burdet E., Caldwell D. G., Carloni R., Catalano M., Eiberger O., Friedl W., Ganeshd G., Garabini M., Grebenstein M., Grioli G., Haddadin S., Hoppner H., Jafari A., Laffranchi M., Lefeber D., Petit F., Stramigioli S., Tsagarakis N., Van Damme M., Van Ham R., Visser L. C., Wolf S.* Variable impedance actuators: A review // Robotics and autonomous systems. — 2013. — Vol. 61, No. 12. — P. 1601–1614.
- Wang W., Fu X., Li Y., Yun C.* Design of variable stiffness actuator based on modified Gear–Rack mechanism // Journal of Mechanisms and Robotics. — 2016. — Vol. 8, No. 6. — P. 061008.
- Wolf S., Grioli G., Eiberger O., Friedl W., Grebenstein M., Höppner H., Burdet E., Caldwell D., Carloni R., Catalano M., Lefeber D., Stramigioli S., Tsagarakis N., Van Damme M., Van Ham R., Vanderborght B., Visser L. C., Bicchi A., Albu-Schäffer A.* Variable stiffness actuators: Review on design and components // IEEE/ASME transactions on mechatronics. — 2015. — Vol. 21, No. 5. — P. 2418–2430.
- Yang H. P., Jang C. S., Van Der Kooij H.* Increasing variable stiffness actuator-response using an electromagnetic spring // 2019 IEEE 4th International Conference on Advanced Robotics and Mechatronics (ICARM). — IEEE, 2019. — P. 7–11.
- Yang Z., Li X., Chen R., Shang D., Xu J., Yang H.* Dynamic performance analysis of the variable stiffness actuator considering gap and friction characteristics based on two-inertia-system // Mechanism and Machine Theory. — 2022. — Vol. 168. — P. 104584.
- Zhang M., Fang L., Sun F., Sun X., Gao Y., Oka K.* Realization of flexible motion of robot joint with a novel permanent magnetic spring // 2018 IEEE International Conference on Intelligence and Safety for Robotics (ISR). — IEEE, 2018. — P. 331–336.
- Zhang M., Ma P., Sun F., Sun X., Xu F., Jin J., Fang L.* Dynamic modeling and control of antagonistic variable stiffness joint actuator // Actuators. — MDPI, 2021. — Vol. 10, No. 6. — P. 116.